Intergranular Strain Evolution in a Zircaloy-4 Alloy with Basketweave Morphology

E. GARLEA, B. CLAUSEN, E.A. KENIK, D. CIURCHEA, S.C. VOGEL, J.W.L. PANG, and H. CHOO

A Zircaloy-4 alloy with Widmanstätten-Basketweave microstructure has been used to study the deformation behavior at the grain level. The evolution of internal strain and bulk texture is investigated using neutron diffraction and conventional microscopic techniques. The macroscopic behavior and intergranular strain development, parallel and perpendicular to the loading direction, were measured *in situ* during uniaxial tensile loading. It was observed that twinning plays a major role in both microstructural changes and polycrystalline plasticity.

DOI: 10.1007/s11661-010-0182-x
© The Minerals, Metals & Materials Society and ASM International 2010

I. INTRODUCTION

ZIRCALOY-4 (ATI Wah Chang, Albany, OR) alloys are extensively used in the nuclear industry as fuel sheathing because of their high-performance under severe pressure and temperature conditions, coupled with high transparency to thermal neutrons. Zircaloy-4 (Zr-4) alloys are polycrystalline zirconium base alloys, with hexagonal-close-packed (hcp) crystalline structure at room temperature. Materials with hcp crystal structure are prone to develop intergranular strains during deformation, as they can exhibit highly anisotropic properties at the grain level.[1,2]

The active modes during plastic deformation for hcp materials have been reported to largely depend on the combined effect of temperature, stress level, bulk texture, and on the c/a ratio.[1–5] The c/a ratio varies from material to material and can be smaller or larger than the ideal sphere packing ($c/a = 1.633$). For Zr alloys, with $c/a = 1.593$ and exhibiting equiaxed microstructure, the prism slip along the $\langle a \rangle$ direction is the most dominant slip system. Deformation with $\langle c \rangle$ components has been observed to be accommodated by twinning on the first- and second-order pyramidal planes. However, slip with $(c + a)$ type Burgers vectors has been often employed to explain the observed ductility of zirconium alloys.[3,5]

Slip and twinning often occur simultaneously, and their interaction is very complicated and less investigated for zirconium alloys with Widmanstätten-Basketweave morphology.[6] The basketweave morphology is significantly different from the typical equiaxed microstructure and it is typical for brazed zones of the CANDU nuclear fuel rods where brazing takes place in the β phase.[6,7] The phase transformation from the β (bcc) phase to the α (hcp) phase occurs with the following Burgers relationships: $\{011\}_\beta$ plane is parallel to the close-packed $(0001)_\alpha$, and a nearest neighbor $\langle 1\bar{1}1 \rangle_\beta$ direction is parallel to a nearest $\langle 11\bar{2}0 \rangle_\alpha$ direction.[8,9] The phase transition is believed to take place by a martensitic mechanism, exhibiting 12 equivalent lattice variants in the α phase.[8] The shape variation from β to α phase occurs *via* plastic deformations accommodated by the Bain strain, which involves prism slip and tensile and compressive twinning.[9,10]

Given the complicated behavior of the alloy, a combination of experimental methods sensitive to crystallographic orientation, such as neutron diffraction and microscopy, need to be employed to understand the polycrystalline plasticity of such a microstructure and its implication to the material performance. Neutron diffraction is a suitable technique to correlate the bulk behavior to grains' internal strain and orientation and to measure the elastic lattice strain response to external factors (*e.g.*, stresses and environments).[11,12]

In this article, the intergranular strains developed under uniaxial tensile loading and the texture evolution were studied by *in-situ* neutron diffraction of a martensitic Zircaloy-4 alloy with basketweave morphology. The polycrystalline plasticity and the major deformation modes of the Zr-basketweave morphology are discussed

E. GARLEA, formerly Graduate Student with the Department of Materials Science and Engineering, The University of Tennessee, Knoxville, TN 37996, is now Technical Staff Member at Y-12 National Security Complex, with Applied Technologies Division, Y-12 National Security Complex, Oak Ridge, TN 37831. Contact e-mail: garleae@y12.doe.gov B. CLAUSEN, Technical Staff Member, SMARTS Instrument Scientist, and S.C. VOGEL, Technical Staff Member, HIPPO Instrument Scientist, are with the Lujan Center (LANSCE-LC), Los Alamos National Laboratory, Los Alamos, NM 87545. E.A. KENIK, Technical Staff Member, and J.W.L. PANG, Research Scientist, are with the Materials Science and Technology Division, Oak Ridge National Laboratory, Oak Ridge, TN 37831. D. CIURCHEA, Professor, is with the Department of Physics, Babes-Bolyai University, Cluj-Napoca, 400084, Romania. H. CHOO, Associate Professor, is with the Department of Materials Science and Engineering, The University of Tennessee, Knoxville and Joint Faculty, with Neutron Scattering Science Division, Oak Ridge National Laboratory, Oak Ridge, TN 37831.

This article is based on a presentation given in the symposium "Neutron and X-Ray Studies of Advanced Materials," which occurred February 15–19, 2009, during the TMS Annual Meeting in San Francisco, CA, under the auspices of TMS, TMS Structural Materials Division, TMS/ASM Mechanical Behavior of Materials Committee, TMS: Advanced Characterization, Testing, and Simulation Committee, and TMS: Titanium Committee.

Article published online March 17, 2010

based on the observed behavior of six different families of grains, microstructural changes, and texture development during uniaxial tension.

II. MATERIAL AND MICROSTRUCTURE

For this study, a commercial zirconium alloy, Zircaloy-4 (Zr-4), was used. The nominal chemical composition (weight percent) of the starting Zr-4 is 1.5Sn, 0.22Fe, 0.12Cr, 0.13O, 0.33Fe-Cr, and balance Zr.[13] The specimens for optical metallography were mechanically polished to 800 grit size followed by etching with a solution of 100 mL glycerin [$C_3H_5(OH)_3$], 10 mL nitric acid (HNO_3), and 5 mL hydrofluoric acid (HF). To enhance the structural effects (*e.g.*, twins), an anodizing process has been employed, using a solution of 60 mL ethanol (C_2H_6O), 25 mL distilled water, 20 mL glycerin, 10 mL lactic acid ($C_3H_6O_3$), 5 mL phosphoric acid (H_3PO_4), and 2 g citric acid ($C_6H_8O_7$) at 50 V for 60 seconds.[14]

The microstructure of the Zr-4 observed under polarized light is presented in Figure 1, showing a typical Widmanstätten-basketweave morphology that forms during cooling from 998 °C to room temperature as a result of the β to α phase transformation. The boundaries of former β grains with a mean diameter of approximately 700 μm are visible in Figure 1(a). The α-Zr plates, exhibiting the basketweave morphology, are shown at higher magnification in Figure 1(b).

The crystallographic orientation of α-Zr plates was investigated by electron backscattered diffraction (EBSD) of the alloy in the as-received (before deformation) condition. The EBSD patterns were collected slowly (1 to 2 pixels per second, rather than the normal 10 to 40 pixels per second) on an electropolished specimen. Figure 2(a) is a backscattered electron (BSE) image taken using a scanning electron microscope (SEM) of an area that was further investigated by EBSD. Using the color coding shown in Figure 2(b), the

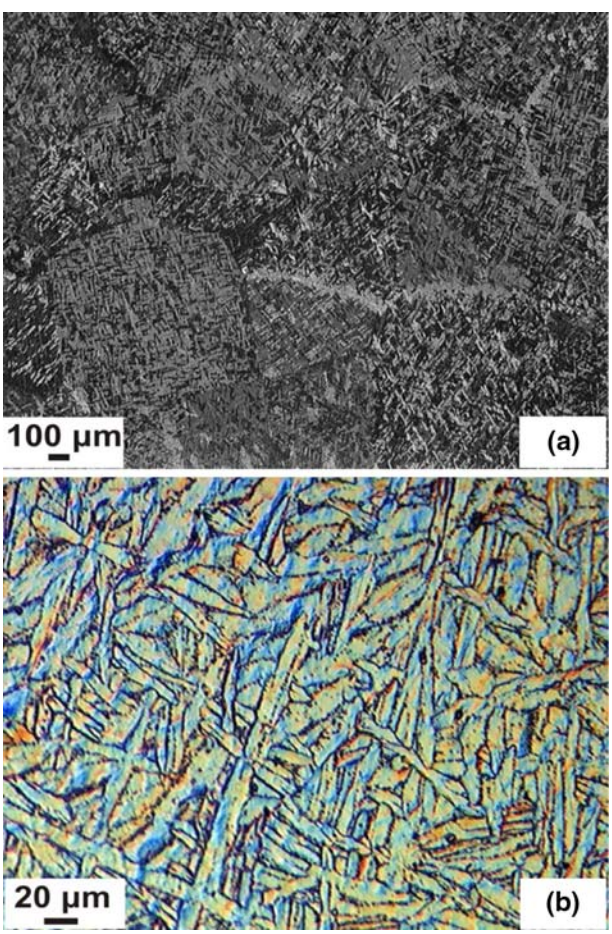

Fig. 1—Polarized light optical microstructure of mechanically polished and etched Zircaloy-4 showing the (*a*) Widmanstätten-Basketweave type structure including the former β-Zr grains with a mean diameter of approximately 700 μm and (*b*) α-Zr plates exhibiting basketweave morphology within the former β grain of the martensitic Zircaloy.

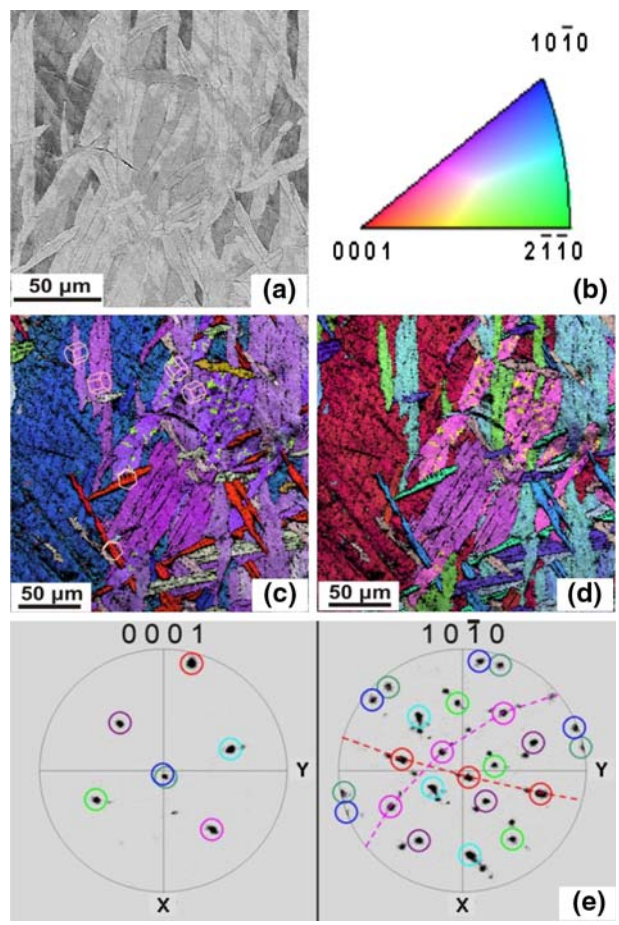

Fig. 2—EBSD characterization of crystallographic orientation of the as-received Zirclaoy-4 α-plates within a former β-grain. (*a*) BSE/SEM image of the area investigated by EBSD. (*b*) The color coding used to obtain the EBSD maps shown in (c) and (d). IPF maps where color represents (*c*) the local crystallographic direction parallel to the foil normal and (*d*) the vertical direction. The schematic unit cells in (c) indicate the local crystallographic orientation of several variants. (*e*) Pole figures for (0001) and $(10\bar{1}0)$ poles, respectively. The colored circles indicate the location of the relevant poles for several of the dominant variants present. Dashed lines indicate crystallographic zones, *i.e.*, poles perpendicular to the same direction ([0001] in this case). The terms *X* and *Y* refer to the horizontal and vertical directions relative to the SEM and IPF images.

inverse pole figure (IPF) maps of the local crystallographic direction parallel to the sample surface normal and the vertical direction, respectively (Figures 2(c) and (d)), were obtained. Both maps have an overlying grayscale image of the local EBSD pattern image quality (IQ), where darker areas indicate poor quality patterns and higher defect density (*e.g.*, dislocations and boundaries). The BSE/SEM image reveals that there are internal boundaries present in many of the individual variants, even though the IPF maps do not show significant rotation (*i.e.*, color difference) across those internal boundaries. This is explained by the reduction in grain size during transformation from 998 °C to the room temperature when the high-temperature grain splits into smaller ones, which remain aligned. The schematic unit cells in Figure 2(c) indicate the local crystallographic orientation of several pairs of α-variants. By associating the orientation and the shape of the oblong laths (Figure 2(c)) with the color coding in Figure 2(d), it can be seen that the interplating interface is of $\langle a \rangle$ type direction, also reported elsewhere.[9] Figure 2(e) presents pole figures for the (0001) and $(10\bar{1}0)$ poles. The colored circles are the location of the relevant poles for several of the dominant variants present. Dashed lines indicate crystallographic zones, *i.e.*, poles, perpendicular to the same direction ([0001] direction in this case). It is possible to identify at least 11 of the 12 α-variants that should be present using the information in both IPFs.[8]

III. INTERGRANULAR STRAIN AND TEXTURE MEASUREMENTS DURING UNIAXIAL TENSILE TESTING

The strain and texture measurements were conducted on a cylindrical tensile specimen with the total length of 101.6 mm, gage length of 19.05 mm, and gage diameter of 6.35 mm, using the Spectrometer for Materials Research at Temperature and Stress (SMARTS) instrument[15] and the High-Pressure Preferred Orientation (HIPPO) instrument,[16] respectively, at the Lujan Center, Los Alamos National Laboratory. Using the SMARTS instrument, uniaxial tensile loads were applied to the Zr-4 tensile specimen, and the internal strain evolution was measured *in situ* using the setup schematically shown in Figure 3. While bulk strain on the sample was monitored using an extensometer, the intergranular strains were obtained from neutron diffraction data collected at certain applied load intervals. The diffraction gage volume employed for this study was defined by the incident beam width of 6 mm and height of 8 mm, and no collimation on the diffracted beam. The loading axis is horizontal at 45 deg to the incident beam, allowing simultaneous measurements of lattice-plane spacings (d-spacings), both parallel (longitudinal direction) and perpendicular (transverse direction) to the loading direction, in the opposing 90 deg detector banks. The tensile test was carried out under strain control, and the lattice strain was measured to a total macroscopic (extensometer) strain of 7 pct (close to failure). The d-spacings for several individual *hkil*

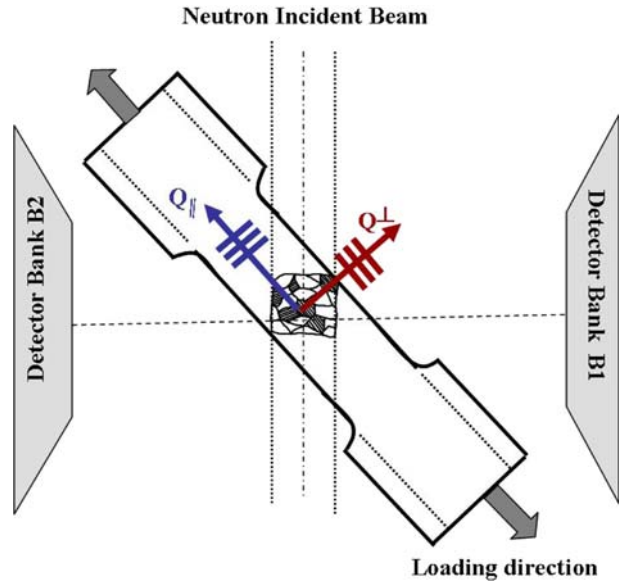

Fig. 3—Schematic representation of the *in-situ* neutron diffraction experiment setup at the SMARTS instrument. The uniaxial tensile loading direction and the detector bank positions allow strain measurement in longitudinal (plane normal parallel to the loading direction, $Q_{\parallel}$) and transverse (plane normal perpendicular to the loading direction, $Q\perp$) directions.

reflections were obtained at each load by single peak fitting, using the General Structure Analysis System (GSAS),[17] and the strain for these reflections, ε_{hkil}, was calculated using

$$\varepsilon_{hkil} = (d_i - d_0)/d_0 \qquad [1]$$

where d_i and d_0 are the d-spacing parameters of the strained and unstrained conditions, respectively. The first data point, before any load is applied, was considered the unstrained condition (d_0), and therefore the presented results do not include the thermal residual strains pre-existing in the specimen.

The texture of the Zr-4 alloy was measured using the HIPPO instrument[16] before and after the applied uniaxial loading. Details of the instrument and the technique for determining the texture are described elsewhere.[18,19] In short, textures are derived from a total of 98 neutron diffraction patterns, which are fitted simultaneously using Rietveld refinement,[20] as implemented in GSAS.[17] The fitting program employs the spherical harmonic method[21] to describe the texture.

IV. *IN-SITU* NEUTRON DIFFRACTION RESULTS AND DISCUSSION

Figure 4 shows six pole figures of the Zircaloy alloy prior to loading including two prism poles $(10\bar{1}0)$ and $(11\bar{2}0)$; the basal pole (0001); and three pyramidal poles $(10\bar{1}1)$, $(10\bar{1}2)$, and $(10\bar{1}3)$, respectively. None of these pole figures show intensity variation above 1.5 or below 0.5 multiples of random distribution, indicating a very weak initial texture. The texture measurement was conducted without any symmetry assumptions with the loading axis at the center of the pole figure. After the

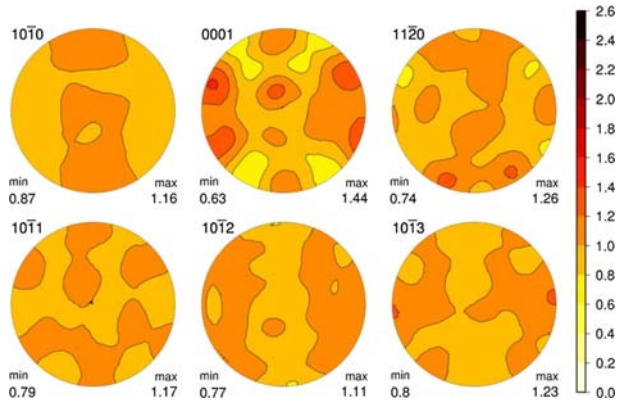

Fig. 4—Initial texture of the as-received Zircaloy-4 alloy measured by neutron diffraction using the HIPPO instrument, without any symmetry assumptions. It shows a near random texture typical for the basketweave α-hcp Zr.

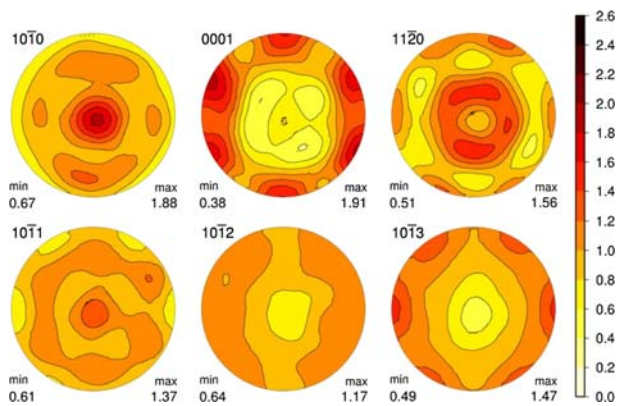

Fig. 5—Texture measured by neutron diffraction using the HIPPO instrument after the tensile test (7 pct total strain). It shows an increase of prism pole intensity close to the center of the pole figure and an increase of basal pole intensity at the perimeter of the pole figure.

tensile loading to 7 pct total strain, the texture developed in the bulk was measured again and the pole figures for the six reflections are depicted in Figure 5. Given the low degree of plastic deformation applied, the texture becomes significantly sharper. An increase in $(10\bar{1}0)$ pole density is observed at the center of the pole figure, due to the reorientation of plates in the tensile direction; accordingly, the (0001) pole figure has the initial sixfold symmetry intensified. The change of the basal pole figure is a decrease at the center accompanied by an increase along the perimeter, with not much change in the remaining parts of the pole figure. The $(11\bar{2}0)$ pole figure has its center nearly unchanged, but a ring of higher density developed around it. The prism poles and the basal pole exhibit a correlated behavior involving a rotation of about 90 deg, which is consistent with tensile twinning deformation.[3] If compressive twinning would occur, a rotation of the plates of approximately 60 deg should have taken place, which would have led to a rotation of basal pole intensity away from the perimeter of the pole figure.

The macroscopic stress-strain curve for uniaxial tension, performed during the neutron experiment for

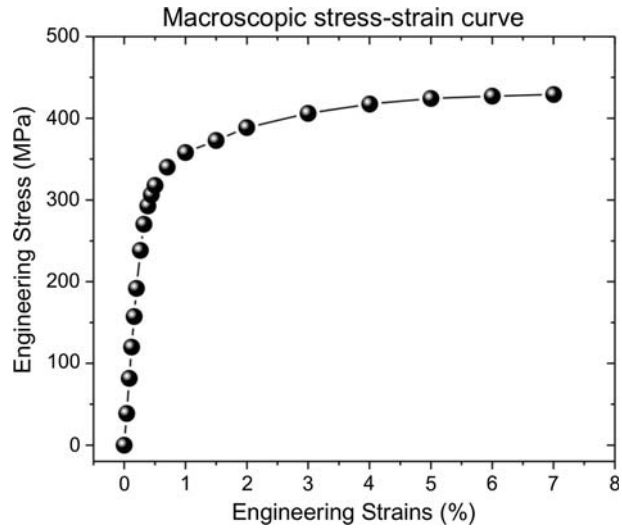

Fig. 6—Macroscopic tensile stress-strain curve measured during the *in-situ* neutron diffraction experiment. The symbol represents the location where neutron data have been collected for the internal strain study.

the hcp Zr-4 alloy, is shown in Figure 6. The symbols represent the time-averaged stress/strain locations where neutron data was recorded for the internal strain study. The macroscopic behavior indicates the bulk elastic modulus (E), the elastic limit, and the 0.2 pct yield stress (σ_y) to be about 100 GPa, 190 MPA, and 318 MPa, respectively.

The measured *in-situ* elastic lattice-strain evolution for six zirconium reflections, in the longitudinal and transverse directions, is presented in Figures 7(a) and (b), respectively. It is worth mentioning that data for many more reflections were obtained; however, for clarity, we are showing only six. The chosen reflections correspond to two prism planes, Zr $(10\bar{1}0)$ and Zr $(11\bar{2}0)$, the basal plane, Zr (0002), and three pyramidal planes, Zr $(10\bar{1}1)$, Zr $(10\bar{1}2)$, and Zr $(10\bar{1}3)$. Also in Figure 7, the macroscopic elastic limit (190 MPa) and the 0.2 pct yield stress (318 MPa) are marked. In the elastic regime, the lattice strains exhibit nearly isotropic behavior for all reflections in both directions. In the plastic regime, the internal strains manifest strongly anisotropic and nonlinear behavior, as the plastic strain component is starting to act. In particular, the longitudinal Zr (0002) has an abrupt deviation from linearity at about 250 MPa, exhibiting a significant decrease in the elastic strain accumulation (Figure 7(a)). This vertical trend and the observed texture developed suggest that these grains, with their c-axis orientated favorably with respect to the loading direction, are yielding through activation of the tensile twinning. The rest of the five families of grains continue to increase their elastic strain accumulation as they now carry the extra load shed by the yielding (0002) grains. As the plastic regime is entered, all six orientations start to deform plastically. Interestingly, above approximately 350 MPa, the pyramidal grains exhibit a similar trend with the basal lattice strain, but not as pronounced. Specifically, the Zr $(10\bar{1}2)$ develops the significant vertical slope, followed

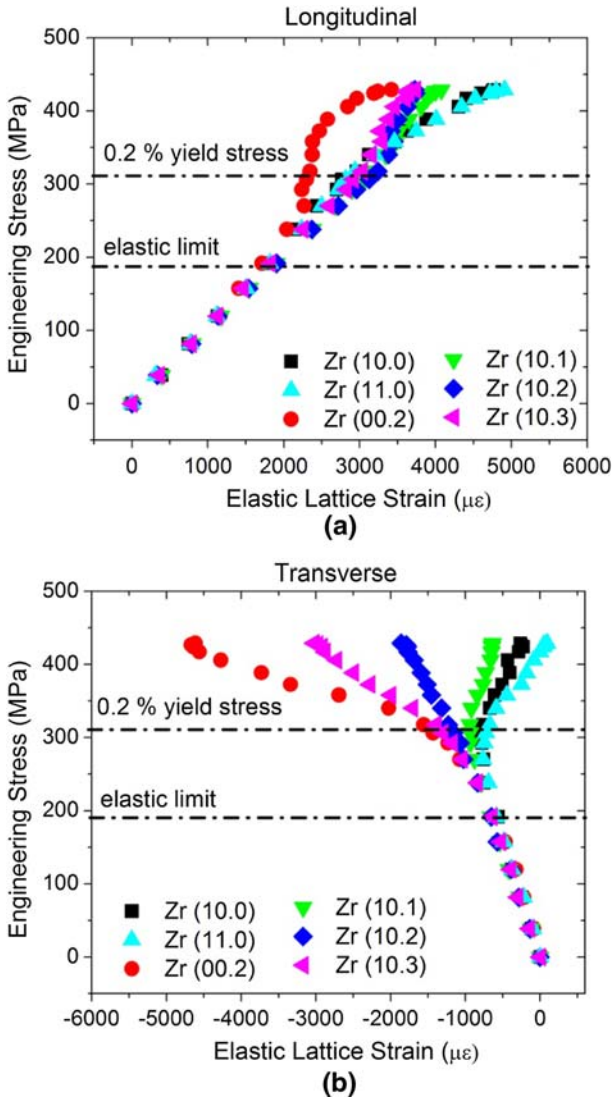

Fig. 7—Neutron diffraction elastic lattice strain evolution under the macroscopic applied tensile load for (*a*) longitudinal and (*b*) transverse directions. The accentuated plastic anisotropy of the hcp Zircaloy is visible.

by Zr $(10\bar{1}1)$ and Zr $(10\bar{1}3)$, whereas the prism planes are the plastically hard planes that show a steady increase in elastic strain. On the other hand, when the pyramidal planes are yielding, the basal grains start loading again. This observed behavior can be explained by activation of other systems. Once the twinning occurs, the lattice rotation re-establishes orientations that may be favorable for other deformation systems that might not have been active otherwise.[3]

In the transverse direction, Zr (0002) and Zr $(10\bar{1}3)$ lose the linear behavior at yield stress (318 MPa). The Zr $(10\bar{1}2)$ has a somewhat vertical trend in the plastic regime, while Zr $(10\bar{1}1)$ and the prism planes, Zr $(10\bar{1}0)$ and Zr $(11\bar{2}0)$, exhibit a significant slope reversal at about 280 MPa. In this respect, it is important to note that the thermal residual stresses present in the alloy at room temperature are not included in the reported lattice strains.

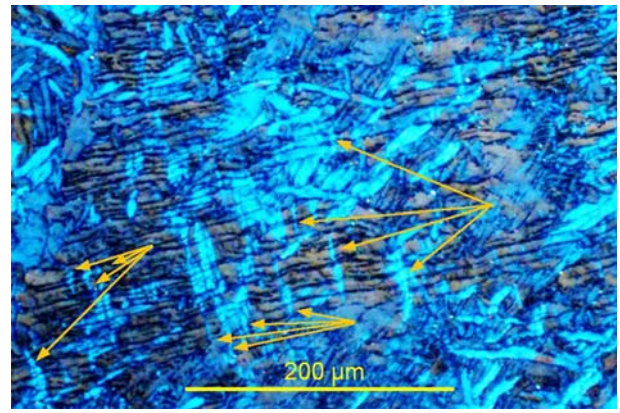

Fig. 8—Optical micrograph of the deformed Zircaloy-4 specimen taken under polarized light after etching and anodizing. The presence of deformation twins is shown by the vertical lenticular features that traverse through the weaved plates.

The deformed specimen was etched and anodized and further studied using an optical microscope with polarized light in order to find evidence of the deformation twins. Figure 8 shows such a micrograph where the lenticular deformation twins are identified. It can be observed that they are perpendicular to the (weaved) transformation twin plates.

The texture developed due to the tensile deformation suggests that tensile twinning is a significant deformation mechanism in this case, supported by the metallographic observation of the deformation twins. In addition, the significant increase in slope of the Zr (0002) lattice strain is also consistent with tensile twin activity, as it would provide relaxation of the elastic strain along the *c*-axis. In turn, this behavior would cause a discrete change of the basal pole intensity, depleting the center of the pole figure and increasing its rim.

V. CONCLUSIONS

The deformation behavior of a Zircaloy-4 alloy with a Widmanstätten-Basketweave microstructure was investigated. Neutron diffraction was used to measure the intergranular strain evolution and the bulk texture developed under uniaxial tensile loading. Six *hkil* reflections were studied closely, namely, two prism, the basal, and three pyramidal reflections. EBSD and optical microscopy with polarized light were employed to study the initial microstructure and to identify deformation modes.

The present study suggests that tensile twinning is a significant deformation mechanism in the case of martensitic Zircaloy-4 with basketweave morphology.

ACKNOWLEDGMENTS

One of the authors (EG) acknowledges the support of the National Science Foundation International Materials Institutes Program (Grant No. DMR-0231320),

Tennessee Advanced Materials Laboratory (TAML) Fellowship Program, and thanks Professor P.K. Liaw, University of Tennessee, for his guidance. EG also acknowledges R.L. Bridges, Y-12 National Complex Security, for help with the metallography. This work has benefited from the use of the Lujan Neutron Scattering Center, Los Alamos Neutron Science Center, which is funded by the Office of Basic Energy Sciences (United States Department of Energy (DOE)). Los Alamos National Laboratory is operated by Los Alamos National Security LLC under DOE Contract No. DE AC52 06NA25396. The EBSD analyses were conducted at the ORNL SHaRE User Facility, which is supported by the Division of Scientific User Facilities, Office of Science, DOE.

REFERENCES

1. M.T. Hutchings, P.J. Withers, T.M. Holden, and T. Lorentzen: *Introduction to the Characterization of Residual Stress by Neutron Diffraction*, Taylor & Francis Group, LLC, Boca Raton, FL, 2005, pp. 233–54.
2. U.F. Knock, C.N. Tomé, and H.-R. Wenk: *Texture and Anisotropy, Preferred Orientations in Polycrystals and Their Effect on Materials Properties*, Cambridge University Press, Cambridge, United Kingdom, 1998, pp. 467–510.
3. E. Tenckhoff: *Deformation Mechanisms, Texture, and Anisotropy in Zirconium and Zircaloy*, ASTM, Philadelphia, PA, 1988, pp. 13–19.
4. E. Tenckhoff: *Metall. Trans. A*, 1978, vol. 9A, pp. 1401–12.
5. R.G. Ballinger, G.E. Lucas, and R.M. Pelloux: *J. Nucl. Mater.*, 1984, vol. 126, pp. 53–69.
6. R.A. Holt: *J. Nucl. Mater.*, 1970, vol. 35, pp. 322–34.
7. V. Quach and D.O. Northwood: *Metallography*, 1984, vol. 17, pp. 191–201.
8. H.-R. Wenk, I. Lonardelli, and D. Williams: *Acta Mater.*, 2004, vol. 52, pp. 1899–1907.
9. D. Ciurchea, A.V. Pop, C. Gheorghiu, I. Furtuna, M. Todica, A. Dinu, and M. Roth: *J. Nucl. Mater.*, 1996, vol. 231, pp. 83–91.
10. E.C. Bain: *Trans. Am. Inst. Min. Metall. Eng.*, 1924, vol. 70, pp. 25–46.
11. D.W. Brown, M.A.M. Bourke, B. Clausen, D.R. Korzekwa, R.C. Korzekwa, R.J. McCabe, T.A. Sisneros, and D.F. Teter: *Mater. Sci. Eng. A*, 2009, vol. 512 (1–2), pp. 67–75.
12. E. Garlea, V.O. Garlea, H. Choo, C.R. Hubbard, and P.K. Liaw: *Mater. Sci. Forum*, 2007, vols. 539–543, pp. 1443–48.
13. Wah Chang Company Technical Department, www.wahchang.com.
14. G.F.V. Voort: *Metallography, Principles, and Practice*, McGraw-Hill Book Co., New York, NY, 1984, p. 701.
15. M.A.M. Bourke, D.C. Dunand, and E. Üstündag: *Appl. Phys. A*, 2002, vol. 74 (Suppl. II), pp. S1707–S1709.
16. H.-R. Wenk, L. Lutterotti, and S. Vogel: *Nucl. Instrum. Methods Phys. Res. A*, 2003, vol. 515, pp. 575–88.
17. A.C. Larson and R.B. Von Dreele, "General Structure Analysis System (GSAS)," Los Alamos National Laboratory Report LAUR, 2000, pp. 86–748, http://www.ncnr.nist.gov/xtal/software/gsas.html.
18. S. Matthies, J. Pehl, H.-R. Wenk, L. Lutterotti, and S.C. Vogel: *J. Appl. Cryst.*, 2005, vol. 38 (3), pp. 462–75.
19. S.C. Vogel, C. Hartig, L. Lutterotti, R.B. Von Dreele, H.-R. Wenk, and D.J. Williams: *Powder Diffr.*, 2004, vol. 19 (1), pp. 65–68.
20. H.M. Rietveld: *J. Appl. Cryst.*, 1969, vol. 2, pp. 65–71.
21. R.B. Von Dreele: *J. Appl. Cryst.*, 1997, vol. 30, pp. 517–25.